Spectral replacement using machine learning methods for continuous mapping of Geostationary Environment Monitoring Spectrometer (GEMS)

Yeeun Lee[1], Myoung-Hwan Ahn[1], Mina Kang[1], Mijin Eo[1]

5   [1]Department of Climate and Energy Systems Engineering, Ewha Womans University, Seoul, 03760, Republic of Korea

Correspondence to: Myoung-Hwan Ahn (terryahn65@ewha.ac.kr)

Abstract. Earth radiances in the form of hyperspectral data contain useful information on atmospheric constituents and aerosol properties. The Geostationary Environment Monitoring Spectrometer (GEMS) is an environmental sensor measuring such hyperspectral data in the ultraviolet and visible (UV/VIS) spectral range over the Asia-Pacific region. After successful

10   completion of the in orbit test (IOT) of GEMS in October 2020, bad pixels are found as a remaining calibration issue to be updated with follow-up treatment. During the IOT, one-dimensional interpolation is performed in operation to replace the erroneous pixels of GEMS, which causes high interpolation error for a wide defective area on the detector array. To resolve the issue, this study suggests machine learning methods with artificial neural network (ANN) and multivariate linear regression (Linear) for filling in a spectral gap of defective spectra. The basic assumption of the methods is that radiances of a spectrum

15   have linear and non-linear relations and a finite range of radiances could be reproduced with the relations. The machine learning models are trained with normal measurements of GEMS after dimensionality reduction for input parameters with principal component analysis (PCA) for efficient training process. Results show that PCA-Linear has small prediction errors especially for a narrower spectral gap and less vulnerable to outliers in the training data with the prediction error of 0.5-5%. PCA-ANN shows better results emulating strong non-linear relations with the prediction error within 5% except for the shorter

20   wavelengths around 300 nm. The dominant spectral patterns could be successfully reproduced with the models nearly within the level of radiometric calibration accuracy of GEMS but limitations still remain particularly in the reproduction of the precise spectral features which needs additional information to be investigated further. As the initial approach reproducing missing radiances of GEMS, this study verifies that spectral relations in the UV/VIS spectrum are successfully reproduced with a simple machine learning model, which has high potential to be updated further for enhancing measurement quality of

25   environmental satellite measurements. ~~The results show that defective radiances at the wavelengths of strong absorption lines is better replaced with PCA-ANN with the error of 5%, while PCA-Linear is better for reproducing radiances having strong correlation with input radiances. The shorter the spectral range of output radiances is, the smaller the prediction error is with PCA-Linear (0.5-5%). Spectral and spatial discontinuity caused by real bad pixels can be significantly improved with the trained machine learning models especially for wide defect areas. This study verifies that spectral relations of radiances in the~~

30 ~~UV/VIS spectrum are successfully reproduced with a simple machine learning model, which has high potential to be investigated further for enhancing measurement quality of environmental satellite measurements.~~

1 Introduction

Earth radiance contains useful information on the chemical composition in the atmosphere, especially when it is measured in the form of many contiguous spectral bands. This type of measurement is referred to as 'hyperspectral' (Bovensmann et al., 1999; Goetz et al., 1985), because it is frequently sampled with high spectral resolution to accurately describe absorption lines of a targeted gaseous or particulate component (Boersma et al., 2004; Kang et al., 2020; Manolakis et al., 2019; Pan et al., 2017). The Geostationary Environment Monitoring Spectrometer (GEMS) on-board the Geostationary Korea Multi-Purpose Satellite-2B (GEO-KOMPSAT-2B) is an environmental sensor providing such a hyperspectral measurement in the ultraviolet and visible (UV/VIS) spectral region from 300 to 500 nm with a spectral resolution of finer than 0.6 nm (Kim et al., 2020). Following the launch of the satellite in February 2020, the in orbit test (IOT) of GEMS was successfully completed in October 2020 with some issues to be continuously monitored. The root cause of each issue is to be examined with collected long-term measurements, as it has been dealt with for other polar orbit sensors having similar sensor characteristics (Ludewig et al., 2020; Pan et al., 2019, 2020; Schenkeveld et al., 2017).

One of the issues to be periodically monitored is about bad pixels, which refer to anomalous pixels having hot, cold, noisy or drifted readout values in raw data (Ló´pez-Alonso and Alda, 2002). The definition of bad pixels is not universal, and in this paper, it refers to all kinds of pixels presenting abnormal observation features. Bad pixel detection is based on sensor characterization by sorting out erroneous signals from normal trend. A few hot pixels were flagged as bad pixels during on-ground tests for GEMS and additional pixels have been sorted out during the IOT because of the impacts from the launch of the satellite and different environment conditions in space. The number of bad pixels tends to increase as time goes by (Kieffer, 1996), which indicates a significant number of bad pixels could affect ~~to~~ the measurement quality during the operation period of GEMS.

Following the bad pixel detection, replacement of measurements on bad pixel positions needs to be performed. There are various ways to replace the measurements on bad pixels (Boldrini et al., 2012; Burger, 2009; Rankin et al., 2018), and in the GEMS calibration system, it adopts one-dimensional spatial interpolation on the detector (Fischer et al., 2007; Schläpfer et al., 2007). However, the approach showed its limitation during the IOT, when an area consisting of bad pixels is quite large and the adjacent pixels valid for spatial interpolation are too far from the erroneous area. Especially, when a scene on the Earth dramatically changes, discontinuity caused by the interpolation becomes larger. This phenomenon affects ~~to~~ not only spatial discontinuity on two-dimensional measurements, but also to a retrieval process using the spectral features contaminated by bad pixels (Marchetti et al., 2019).

In this respect, this study suggests machine learning methods to replace bad pixels on the radiance level using valid spectral features of normal measurements. As a way of replacement, we compare machine learning approaches using artificial

neural network (ANN) and multivariate linear regression. Theoretically, it has been verified that ANN can accurately emulate non-linear relations with a simple model structure when there are a large number of training data (Cybenko, 1989; Hornik et al., 1989). Machine learning methods have a high chance to successfully process hyperspectral data because the abundant datasets make training process more effective after breaking the curse of dimensionality with a proper pre-processing step (Gewali et al., 2018). Principle component analysis (PCA) is applied in this study, as it is useful to extract important information from hyperspectral measurements (Bajorski, 2011).

For atmospheric remote sensing, the majority of researches on hyperspectral measurements has employed machine learning as a proxy of the radiative transfer model to retrieve geophysical states with measured spectral radiances (Hedelt et al., 2019; Loyola et al., 2018; Zhu et al., 2018). There are fewer approaches applied to obtain radiation flux (Dorvlo et al., 2002; Zarzalejo et al., 2005) and even much fewer to obtain hyperspectral radiances for different purposes such as to accurately quantify radiative forcing in climate system (Taylor et al., 2016), increase spectral resolution (Le et al., 2020) and fill in a spectral gap for inter-calibration (Wu et al., 2018). A monochromatic radiance itself rarely contains any important meaning and thus seldom has it been a final target for machine learning. In this study, however, radiance at each wavelength of a targeted spectral region becomes an important output to be reproduced. Considering that the retrieval process is based on the measured spectral features, how much information could be reproduced with the machine learning methods also needs to be quantified.

The following sections are organized as follows. Section 2 introduces sensor specification of GEMS including an overview of bad pixel detection and replacement methods for GEMS. In the section, a general description of machine learning models suggested in this study is introduced as well as the model structure and hyperparameter setting. Section 3 contains model optimization results and error analysis for wide defect regions. With the optimized model, the spatial and spectral inspection is performed to actual measurements including bad pixel areas. ~~bad pixel replacement is performed to real spectra contaminated by bad pixels and it is compared with linear interpolation, the operational method for replacing bad pixels of GEMS.~~ In Sect. 4, conclusions are presented with limitations as well as further applications in the future study.

2 Data and methods

2.1 Data description

2.1.1 GEMS

GEMS is a UV/VIS imaging spectrometer in the geostationary orbit observing the Asia-Pacific region (5° S-45° N, 75° E-145° E) with high spatial and spectral resolution to retrieve key atmospheric constituents such as ozone (O_3), sulfur dioxide (SO_2), nitrogen dioxide (NO_2), formaldehyde (HCHO), glyoxal (CHOCHO) ~~O_3, SO_2, NO_2, HCHO~~ and aerosol properties (Level 2) (Kim et al., 2020). The observation targets of GEMS are the Sun (irradiance mode) and the Earth (radiance mode) and the description for each measurement mode is summarized in Table 1. In both measurement modes, incident light from a scene passing through a fore-optics and a spectrometer reaches to a two-dimensional detector array, the charge-coupled device (CCD)

detector. The CCD of GEMS comprises 2,048 rows and 1,033 columns of photoactive pixels along the spatial direction from north to south (N-S) and the spectral direction with a sampling interval of 0.2 nm, respectively. GEMS observes the Sun on the purpose of calibration once a day with a premise of the measured solar irradiance being stable and nearly time independent. For Earth measurements, GEMS measures the backscattered radiation from east to west about 700 times by moving a scan mirror and for each scan, totally 2048 pixels are obtained along the north-south direction. All measurements at each scan position are combined together to cover the full field of regard (FOR) of GEMS. GEMS scans the earth around 700 times within 30 minutes from east to west to cover the full field of regard (FOR) of GEMS. In both measurement modes, incident light from a scene passing through a fore optics and spectrometer reaches to a two-dimensional detector array, the charge-coupled device (CCD) detector. The CCD of GEMS comprises 2,048 rows and 1,033 columns along the spatial direction from north to south (N-S) and the spectral direction with a sampling interval of 0.2 nm, respectively.

Table 1 Top level measurement specifications of GEMS

Measurement mode	Solar irradiance	Earth radiance
Data dimension [spectral, spatial, scan]	[1033, 2048]	[1033, 2048, 695] (nominal scene)
Spectral range [nm]	300-500	
Spectral sampling [nm/pixel]	0.20	
Spectral resolution [nm]	< 0.60	
Spatial resolution [km^2]	-	3.5×8 (spatial $\times$ scan)
Measurement frequency	Once a day (13:00 UTC)	Every hour (00:45-07:45 UTC)

2.1.2 Bad pixel

Bad pixel detection is generally performed with dark-current measurements which are taken without exposure to light for a certain integration time (Howell, 2006), and for GEMS, the integration time corresponds to about 70 milliseconds. Figure 1 illustrates bad pixel positions (in white) on the GEMS CCD detector array identified during the IOT. A cluster and distinct line shapes of bad pixels shown in Fig. 1a are initially identified during on-ground calibration before the launch of the satellite. Following the suggestions made by the instrument developers, linear interpolation along the spatial (N-S) direction (north-south) is applied to replace the unusable measurements on bad pixel positions. With such a simple procedure, a single bad pixel could be properly substituted. However, it was found during the IOT that significant interpolation error could occur on the bad pixel positions denoted as Defects 1-3 (see Fig. 1b), especially when the spatial width of the invalid area is too wide as shown in Defects 2 and 3.

(a)   (b)
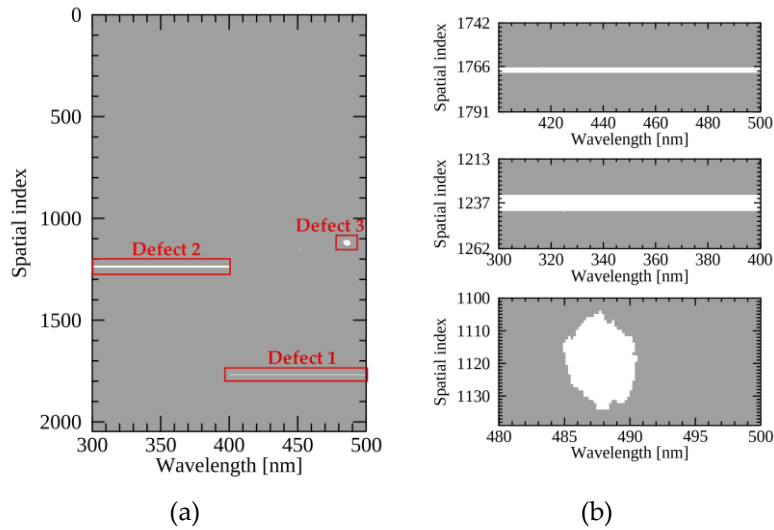
Figure 1 (a) Two-dimensional bad pixel map on the GEMS CCD detector along the spectral (x-axis) and spatial direction (y-axis) and (b) zooming in the bad pixel positions from top to bottom rows for Defects 1-3. Bad pixels are marked in white.

The interpolation error could seriously affect ~~to~~ the Level 2 products of which the spectral fitting windows are overlapped with bad pixel areas. For instance, cloud properties and aerosol effective height (AEH) of GEMS are retrieved from O_2-O_2 absorption bands around 477 nm (Choi et al., 2021; Kim et al., 2021) where the cluster of bad pixels is located (Defect 3). During the IOT, Defect 3 caused spatial discontinuity to the retrieved cloud and AEH distribution, which made the fitting window of the products modified to avoid bad pixel effects. The O_3 retrieval is also affected by Defect 2 (300-400 nm) as the spectral radiances within 300-380 nm provide major information for the O_3 retrieval of GEMS (Bak et al., 2019). The bad pixel effects in the Level 2 product are clearly shown in Fig. 2 which presents radiances at 312 nm and the retrieved total O_3 column of GEMS. Even though radiances at the certain wavelength are homogeneous with its surroundings (see Fig. 2b). The spectral patterns are not properly reproduced with the existed method (spatial interpolation) causing the distinct horizontal line in Fig. 2c.

(a)   (b)   (c)
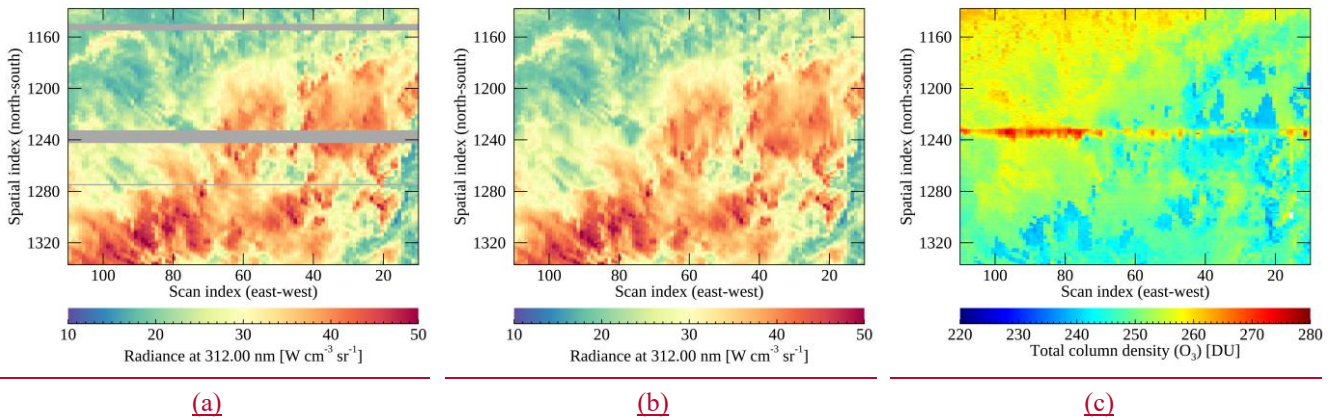
Figure 2 Spatial distribution of radiances at 312 nm with bad pixels (a) marked in dark gray and (b) reproduced with spatial interpolation and (c) the total O$_3$ column of GEMS. The measurements are on 10 March 2021 (06 UTC).

To eliminate the bad pixel effects this study suggests machine learning methods to spectrally reproduce radiances on bad pixels instead of spatial interpolation as described in Fig. 3. The multivariate linear regression and ANN models are compared to evaluate model performance for reproducing Earth radiance corresponding to the bad pixel positions of Defects 1-3. Solar measurements have high spatial homogeneity resulting in small interpolation error even on the large bad pixel areas, and are not considered in this study.
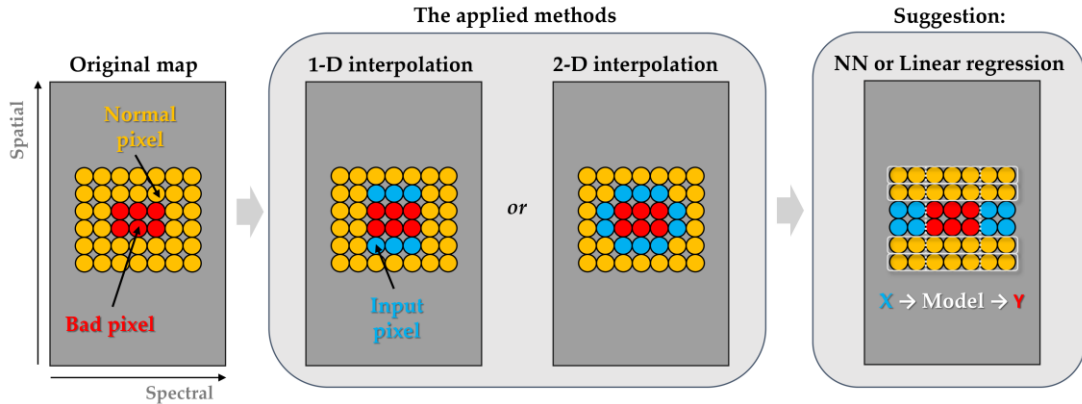
Figure 3 Schematic chart of the input (blue circle) and output pixels (red circle) on the GEMS CCD for the spatial interpolation and machine learning methods suggested in this study. Yellow circle indicates adjacent pixels to bad pixel position.

2.2 Replacement approach

2.2.1 General description

Reproduction of radiances on bad pixels is based on a fact that radiances at different wavelengths for a scene are highly correlated with each other (Liu et al., 2006; Wu et al., 2018). If the relations can be accurately established, some missing values in a spectrum can be properly reproduced with radiances at the other wavelengths. Further questions to be investigated are whether non-linear relations could be accurately emulated with machine learning methods and valid information for the reproduction may exist in the input radiances. To emulate the relations of the input and output radiances in a spectrum, the randomly collected GEMS spectra for various scenes are used which are measured on normal pixels located closer to a bad pixel area on the detector array for Defects 1-3. The basic premise of this approach is that neighbor pixels on the detector array would have similar measurement characteristics. After training a model with the normal spectra, a spectral gap (output radiances) could be reproduced through the model.

Because it is highly possible that input radiances have redundant information, PCA is applied for dimensionality reduction to compress the input radiances to low-dimensional principle components (PCs). The PCA process is given by the following Eq. (1):

$$150 \quad \mathbf{Z}_{n \times p} = \mathbf{X}_{n \times \lambda} \mathbf{W}_{\lambda \times p} \tag{1}$$

where $\mathbf{Z}$, $\mathbf{X}$ and $\mathbf{W}$ represents the PC scores, input and PC matrix, respectively. The PC scores matrix ($\mathbf{Z}$) is obtained by projecting the input to the PC subspaces with $\mathbf{W}$, which is obtained by applying eigenvalue decomposition to the $\mathbf{X}$. The subscript n, λ and p means the dimension of matrix corresponding to the number of datasets, wavelengths and the number of PCs, respectively.

155   With the compressed data, multivariate linear regression (PCA-Linear) and ANN (PCA-ANN) models are trained to define the relations between input ($\mathbf{X_m}$) and output ($\mathbf{Y_n}$) radiances in a spectrum. The PCA-ANN model is constructed with a simple feed-forward model with a hidden layer as described in Fig. 4̶3. In the model optimization process, the PCA-ANN model with a hidden layer showed faster and more effective convergence of loss function than the models having multi-hidden layers in this study. For PCA-Linear, it adopts a simple linear model structure consisting of parameters such as weight and

160   bias having the minimum mean squared error (MSE) between the regressed and measured radiances. After model optimization, it can be used to replace bad pixels ($\mathbf{X'_m}$, $\mathbf{Y'_n}$) with radiances to be likely measured by the sensor.
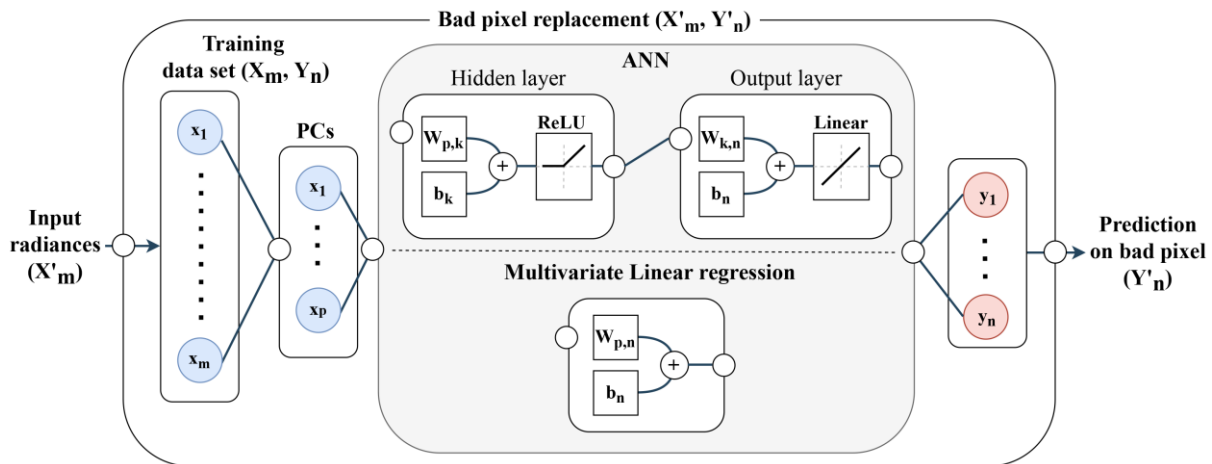
Figure 4̶3 Schematic chart of the training and bad pixel replacement process. $\mathbf{W}$ and $\mathbf{b}$ represent weight and bias parameters in each layer. The subscript m, n, p and k is equal to the spectral dimension of input and output parameters, the number of PCs and hidden nodes of the

165   ANN model, respectively.

2.2.2 Input/Output and model optimization

For the reproduction process, radiances of each spectrum are divided into input and output radiances based on the specified spectral ranges in Table 2. The spectral ranges of output radiances for Defects 1-3 are identical to each defective region and the rest part of a spectrum becomes input radiances. Training and test data are constructed with GEMS radiance data which

170   are randomly sampled out in March-April 2021 to update model parameter and check for overfitting, respectively. The datasets for the models should be sampled at identical spectral grids and for that, each spectrum is interpolated in a pre-processing step and after the reproduction, the spectra are reversely interpolated onto its original spectral grids. Considering that the intrinsic information a spectrum has could be lost during the interpolation processes, the finer spectral grids (0.1 nm) are adopted for

the model to minimize interpolation errors by preserving radiances at more frequent intervals than the original grids. The solar
zenith angle (SZA) and viewing zenith angle (VZA) are key variables determining optical paths of upwelling and downwelling
radiances and thus are used as input variables together with radiances. The neural network constructed with the hyperparameter
setting presented in Table 2 is implemented with TensorFlow, a high-level Application Programming Interface (API) written
in Python. As described in Fig. 4̶3̶, the activation function is the Rectified Linear Unit (ReLU) in the hidden layer of the ANN
model. The structure itself is not complicated but it has multiple nodes in the input and output layers, which makes ReLU more
competitive (Nwankpa et al., 2018). The hyperbolic tangent (tanh) and sigmoid function show poor results especially when
the output parameters have lower variance making the optimization stuck into the averaged value and preventing the model
from being updated.

Table 2 Input and output (I/O) parameters for ANN training and hyperparameter for optimization of neural network.

Model	Parameter	Defect 1	Defect 2	Defect 3	Remark
I/O	Input (X_m)	SZA / VZA		460-483.9 / 491.1-500 nm	Random selection (100,000 for training and test data)
		300-400 nm	400-500 nm		
	Output (Y_n)	400.1-500 nm	300-399.9 nm	484-491 nm	
Hyper-parameter	Activation function	ReLU			
	Optimizer	Adam optimizer			
	Loss function	Mean squared error			
	Scaling	Standardization			

For the optimizer, Adaptive Moment Estimation (Adam) is used which shows stable results compared to Stochastic
Gradient Descent (SGD) and Root Mean Square Propagation (RMSProp) (Kingma and Ba, 2015). It is empirically found that
SGD without gradient clipping tends to cause exploding gradient and RMSProp has difficulty reaching the global minima
compared to Adam. Figure 5̶4̶ presents the converging process of the PCA-ANN model for Defect 2 applying different
optimizers with and without SZA and VZA conditions. The additions of the angle conditions as input parameters speed up the
model convergence with smaller MSE because without the angle parameters, the information would be implicitly elicited
during the optimization process. The model converges with angle conditions at 44, 98 and 33 epochs for Adam, SGD and
RMSprop, respectively. Adam converges at the smallest MSE while the SGD converges with the highest MSE. RMSprop
presents unstable loss for validation data and converges with higher MSE compared to Adam.
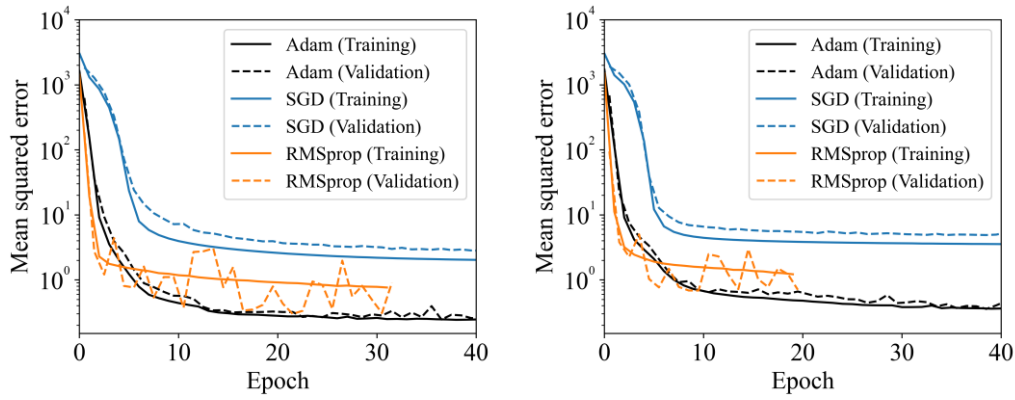
Figure 5 Training and validation losses for Defect 2 (a) with and (b) without the angle conditions as input parameters. The results are obtained with different optimizers such as Adam (black), SGD with the gradient clipping value of 0.5 (blue) and RMSprop (orange).

3 Results and discussion

3.1 ~~Optimization results~~Model selection

3.1.1 Optimization results

Earth radiance is determined by the interactions of light with trace gases, aerosols and clouds in the atmosphere and reflected properties of a scene. The magnitude of a spectrum is dominantly determined by the scene properties which result in strong linear relations among radiances in a spectrum. In other words, when a scene is dark (bright), the upwelling radiances of the scene over the whole spectral region tend to become generally low (high). The PCA analysis performed for dimensionality reduction describes the characteristic with PC scores of input radiances in training data for Defect 2 (See Fig. 6~~5~~). In the figure, it can be found that the first principal component (PC) is highly correlated with the magnitude of a spectrum represented by the radiance at 354 nm. This indicates that strong linear relations among radiances in a spectrum are compressed to the first PC, which has the largest variance. The non-linear properties caused by atmospheric scattering, absorption, different optical paths and sensor noise are projected onto the ~~other~~ subsquent PC subspaces.
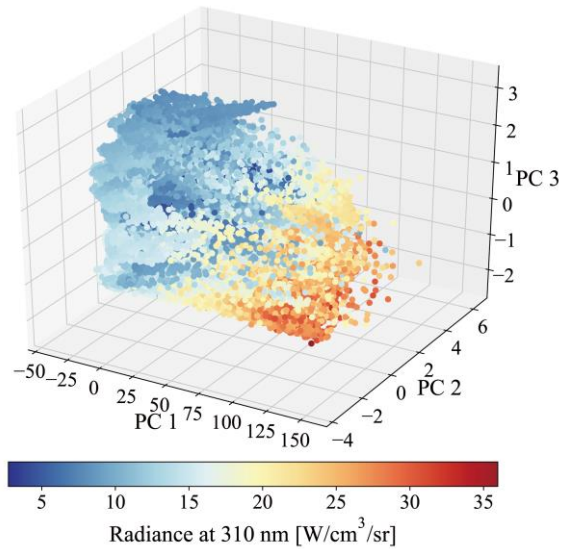
Figure 65 PC scores of input training data from 400 to 500 nm for Defect 2 after dimensionality reduction. Colorbar represents the radiance at 3~~10~~54 nm of output training data.

Figure 7~~6~~ shows model optimization results depending on each model and the number of PCs. Because the spectral range of output radiances differs for each defect region (Defect~~s~~ 1-3), model optimization is performed, respectively. The spectral range~~s~~ of output radiances for Defect~~s~~ 1 and 2 ~~is~~ are wider than that of Defect 3 which results in higher MSE. PCA-ANN seems to be unstable for Defect 1 showing over-fitted features which might be caused by unfiltered outliers in output radiances of GEMS at the wavelengths longer than 480 nm. It is empirically found that PCA-ANN is more vulnerable to outliers compared to PCA-Linear. Defect 2 is at the wavelengths where the upwelling radiances are largely affected by O_3, which increases non-linearity between input and output radiances. Because of the strong non-linearity, PCA-ANN shows better performance than PCA-Linear for Defect 2. Defect 3 has the smallest number of output parameters in a narrow spectral gap which causes strong correlation between input and output radiances. The loss functions (MSE) in Fig. 7~~6~~c are small and converge quickly for both PCA-ANN and PCA-Linear models. With the results, the optimized number of PCs is set to 90 for all defect regions when loss functions for both training and test data efficiently converge, with PCA-Linear for Defect~~s~~ 1 and 3 and the PCA-ANN model for Defect 2.
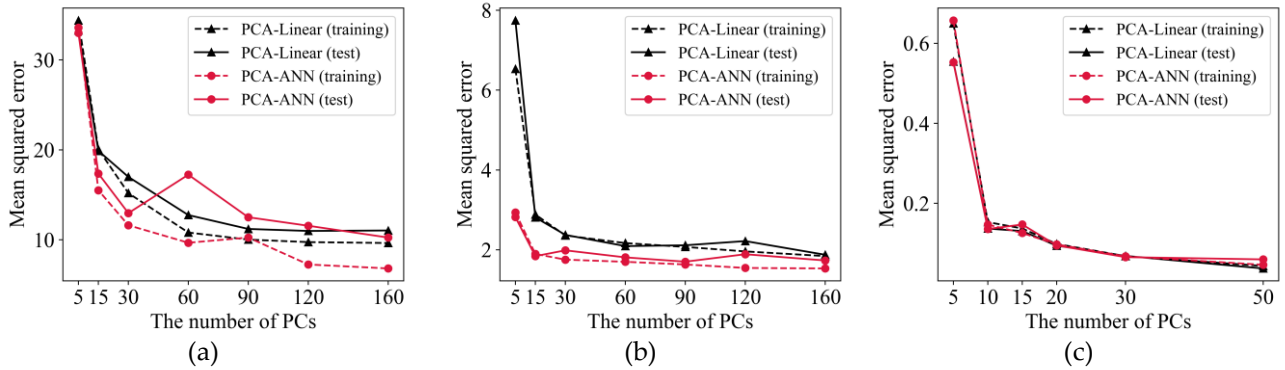
Figure 7~~6~~ Loss function depending on the number of PCs with PCA-ANN (red) and PCA-Linear (black) models to predict the output radiances corresponding to the spectral range of Defect~~s~~ 1-3 ((a): Defect 1, (b): Defect 2 and (c): Defect 3). The dashed and solid line indicates training and test results, respectively. The number of hidden nodes for ANN is double the number of PCs.

3.1.2 Statistical evaluation

~~3.2 Statistical evaluation~~

The optimized model structures for Defect~~s~~ 1-3 are set as described in the previous section. Following that, in this section, model performance is statistically evaluated with training and test datasets specified in Table 2. Figure 8~~7~~ presents mean and normalized root mean squared error (NRMSE) of the predicted output radiances with training and test data. The NRMSE is a statistical indicator normalized by mean radiance at each wavelength and it can be found that radiances affected by strong absorption lines have relatively high uncertainty. Especially, information from the radiances in 400-500 nm is insufficient to properly represent O_3~~ozone~~ absorption features at shorter wavelengths and it causes high uncertainty at the wavelengths shorter than 325 nm in Defect 2. Defect 3 has the smallest NRMSE because of strong linear relations between input and output radiances as previously mentioned in Sect. 3.1. The NRMSE is less than 0.1% for both training and test data for Defect 3. The results show that it is possible to successfully reproduce spectral features at a narrower spectral range with simple linear regression.

(a)

(b)
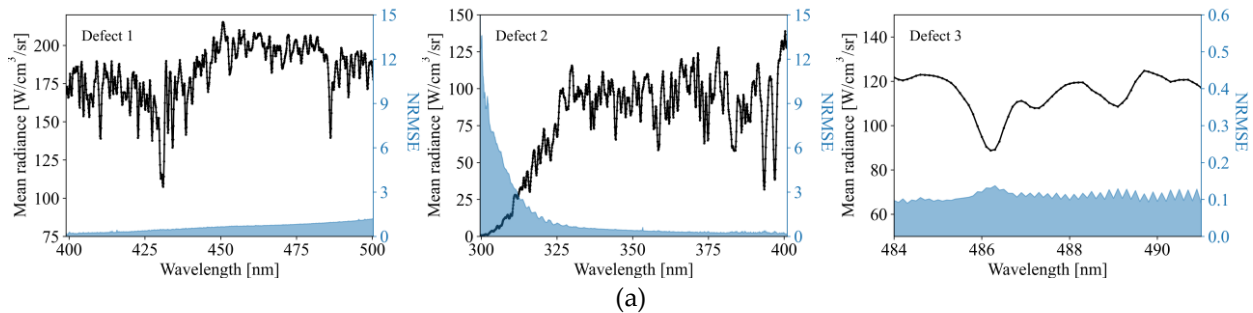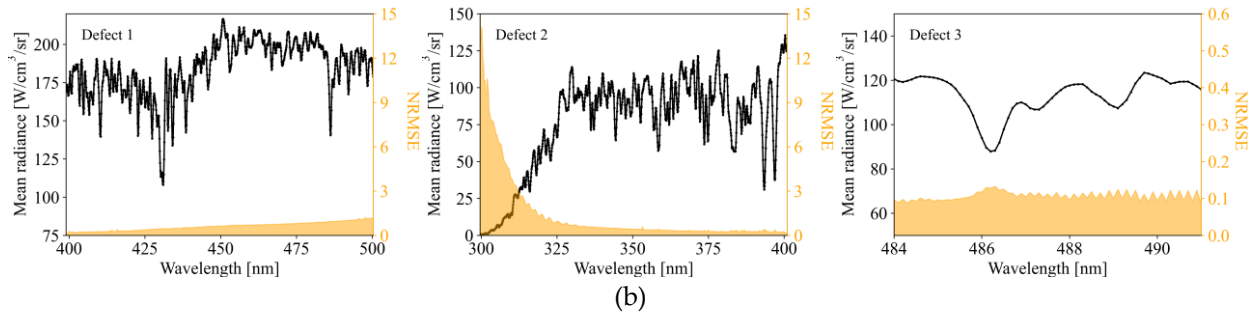
Figure 8~~7~~ Mean (black) and NRMSE (blue) spectra of output radiances for Defect 1-3 with (a) training and (b) test datasets measured in March-April 2021. The unit of NRMSE is percent.

Figure 9~~8~~ shows the error histogram of each prediction model for Defect~~s~~ 1-3 with training and test data. The mode and mean of error histograms are on the order of 0.001-0.01 for test and training data. The machine learning models are good enough to properly emulate spectral relations between input and output parameters, but it is somewhat over-fitted to the training data causing a few outliers for the prediction of test data. Defect 2 has the largest standard deviation, which is consistent with the higher NRMSE at shorter wavelengths around 300 nm in Fig. 8~~7~~. The largest kurtosis of Defect 2 for both training and test data indicates tails of the distributions are heavy compared to normal distribution, mostly from the radiances at shorter wavelengths. Considering that the overall prediction error is within 5% except for the O_3~~ozone~~ absorption lines, the prediction models for Defect~~s~~ 1-3 are well constructed for further bad pixel replacement.

(a)   (b)   (c)
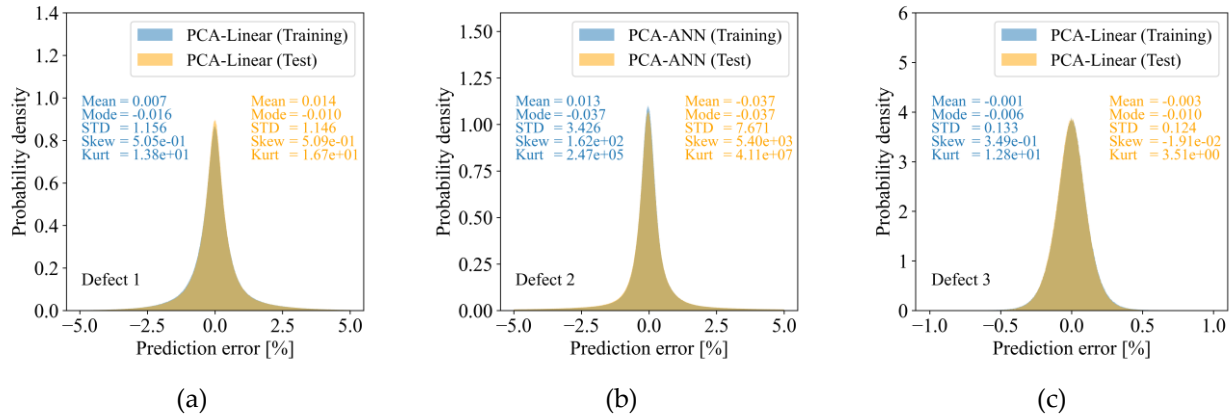
Figure 9~~8~~ Prediction error of randomly collected training (blue) and test (yellow) datasets measured in March-April 2021 with the optimized models for Defect~~s~~ 1-3 (PCA-ANN for Defect 2 and PCA-Linear for Defect~~s~~ 1 and 3). Prediction error and the statistics are~~is~~ calculated with the difference between the predicted and measured radiances divided by the latter.

The training and test datasets presented in Fig~~s~~. 8~~7~~-9~~8~~ are randomly collected spectra of GEMS measurements in March-April 2021, which guarantees a basic assumption in machine learning that the underlying population should be identical for training and test data (Zhen and Li, 2008). However, in operation, the prediction model is obliged to be trained in advance with sufficient datasets for timely reproducing erroneous pixels of satellite measurements on a daily basis. This indicates the assumption might be violated if measurement characteristics of training and test data significantly change. To investigate

further the effect, the prediction model is trained with training and test data measured in March and April 2021, respectively (see Fig. 10~~9~~). The results show that histograms of test data for Defect~~s~~ 1-2 are more skewed than those of training data, when the measurement period~~s~~ of training and test datasets ~~are separated~~differ. On the other hand, prediction results for Defect 3 are~~is~~ independent to the measurement period~~s~~ of training and test data. This results indicate that the spectral features of GEMS spectra change profoundly as time goes by ~~and the changes have strong spectral dependence within 300-500 nm~~.

(a)   (b)   (c)
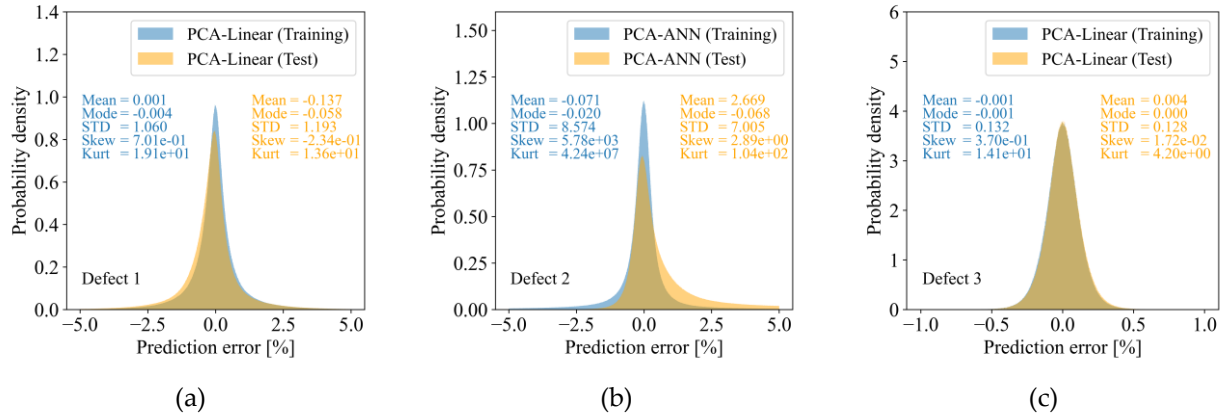
Figure 10~~9~~ Same as Fig. 9~~8~~ with training and test datasets measured in March and April 2021, respectively.

~~**3.3 Application to bad pixel replacement**~~

~~In this section, the prediction model trained with randomly collected spectra in March-April 2021 is employed for reproducing real bad pixels of Defect 1-3 from GEMS measurements on 2 May 2021. It is demonstrated with visual inspection of radiance images and quantitative comparison between machine learning methods and spatial interpolation, the current operational method for bad pixels in the GEMS calibration system. Figure 10 shows earth radiance images of GEMS on a particular region (15° N, 102° E) affected by bad pixels of Defect 3, which has wider spatial width of bad pixels than that of Defect 1-2 along the N-S direction. Spatial discontinuity caused by bad pixels occurs as a horizontal line because GEMS scans the earth from east to west by sequentially recording scan images. Bad pixels of Defect 1-3 are stationary on the detector array, which causes measurements at certain latitudes unavailable. It is also noted that clouds are a main target making spatial discontinuity caused by bad pixels more noticeable with its high spatial variability. The spatial discontinuity is easily found in Fig. 10a because of the bad pixels inaccurately replaced with spatial interpolation. The PCA-Linear for Defect 3 shows better performance because the bad pixel positions easily found in Fig. 10a are entirely indistinguishable in Fig. 10b. The improvement is also found in Defect 2 (not shown), but with its narrower spatial gap compared to Defect 3, the improved results with PCA-ANN for Defect 2 is not visually recognizable. For Defect 1, the spatial width of bad pixels along the N-S direction is narrower (two pixels width along the N-S direction) than that of Defect 2-3, which presents no significant difference between PCA-Linear and spatial interpolation.~~
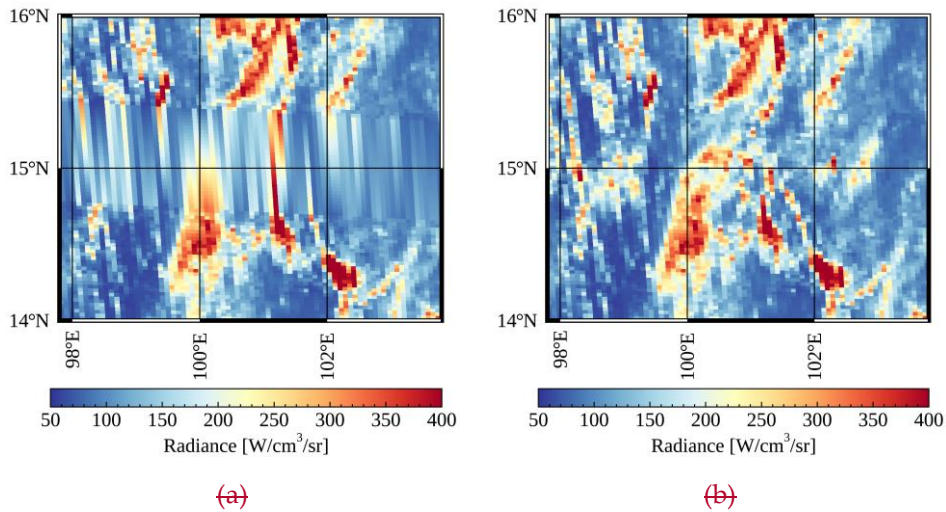
Figure 10 ~~Comparison of bad pixel replacement between (a) spatial interpolation and (b) the machine learning method for the radiance at~~
~~487 nm for Defect 3 measured on 2 May 2021 (03 UTC).~~

~~A closer inspection is performed to analyze the reproduced spectral features for Defect 2-3. In spectral analysis, the~~
~~effectiveness of bad-pixel replacement methods could be well demonstrated at the wavelengths where the input and output~~
~~radiances are met. If the replacement is successful, the partly replaced spectrum should have continuous spectral features over~~
~~the whole spectral range. The spectral range affected by bad pixels for each defect region is 300-400 nm and 484-491 nm,~~
~~which corresponds to the range of output radiances for Defect 2-3, respectively. The rest part of a spectrum is input parameters~~
~~for each defective region. As previously mentioned in Sect. 3.1., PCA ANN shows better performance for Defect 2, while~~
~~PCA-Linear is better for Defect 3 and thus each method is used for Defect 2 and 3, respectively. Figure 11 shows one of~~
~~radiance spectra of Defect 2 and 3 from the GEMS measurement on 2 May 2021. For Defect 3 as shown in Fig. 11b, the~~
~~reproduced spectrum with spatial interpolation shows totally unrealistic features compared to that with PCA-Linear because~~
~~of the wider spatial gap of Defect 3. For Defect 2, however, the reproduced spectra with spatial interpolation and PCA ANN~~
~~show reasonable spectral features and the spectral discontinuity is not clearly discernible at the wavelength of 400 nm.~~

295   To deeply investigate the spectral features of replaced radiances for Defect 2-3, Fig. 12 analyzes reflectance spectra by dividing each radiance spectrum in Fig. 11 with the measured solar spectrum of GEMS. In reflectance, measurement noise from calibration processes could be cancelled out by normalizing earth radiance with measured solar irradiance. The Fraunhofer lines originating from the solar spectrum could also be cancelled out, which makes it easy to analyze spectral features of a spectrum without strong absorption lines. In Fig. 12a, spectral discontinuity with spatial interpolation is more

300   obvious at 400 nm compared to the radiance spectrum in Fig 11a. For Defect 3, Fig. 12b also shows stable features with PCA-Linear at the defective spectral range around 487 nm. It could also be seen that the measurement noise from the sensor could be successfully incorporated in the replaced spectrum with machine learning methods because the measured reflectance would have noise like features if the noise is not properly reproduced in the radiance spectrum. Consequently, the results indicate that the machine learning methods are good enough to properly reproduce spectrally and spatially continuous features using

305   spectral relations of radiances in the UV/VIS spectrum.

(a)   (b)
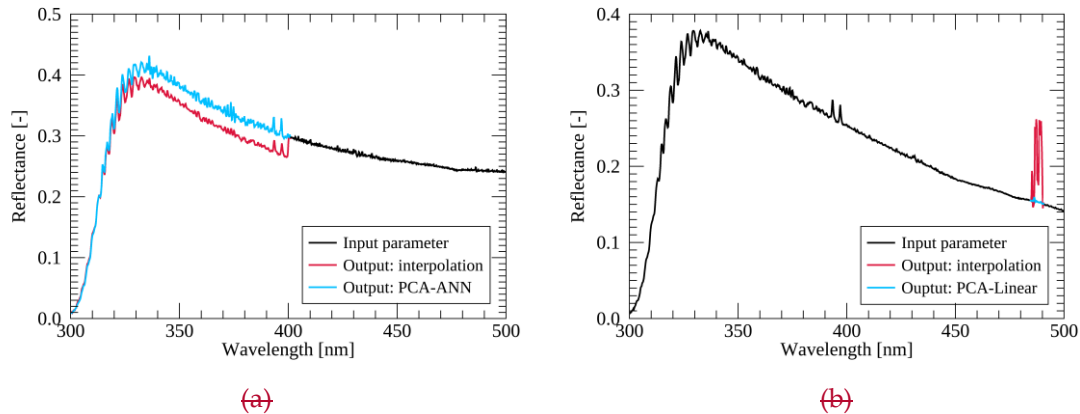
Figure 12 Same as Fig. 11 for reflectance spectrum affected by bad pixels of (a) Defect 2 and (b) Defect 3.

3.2 Evaluation

3.2.1 Spatial and spectral inspection

 For the quantitative evaluation of the reproduced spectra, certain areas are targeted which include each defect (Defects 1-3)

310   and its surroundings where actual measurements regarded as 'true' could be obtained. The evaluation is made with the data measured on 10 March 2021 (06 UTC), which are excluded for the model training. The center longitude of the areas is set to 128° E, which is identical with the sub-nadir longitude of GK-2B. Table 3 presents spectral ranges of Defects 1-3 and the target wavelengths for the analysis. Specifying the wavelengths for the analysis helps to specifically analyze the spectral patterns of absorption lines of trace gases and cloud properties.

315 **Table 3** The spectral range of Defects 1-3 and target wavelengths for the analysis. The third column presents GEMS retrieval products of which each fitting window is overlapped with Defects 1-3.

Defect	Target wavelength	GEMS Level 2 product	Optimized model
1 (400-500 nm)	432-450 nm	CHOCHO, NO$_2$	PCA-Linear
2 (300-400 nm)	312-360 nm	O$_3$, HCHO, SO$_2$, NO$_2$, aerosol optical depth	PCA-ANN
3 (484-491 nm)	484-491 nm	Cloud, AEH	PCA-Linear

The measured and the reproduced radiances with machine learning methods are directly compared, which are hereafter referred to as GEMS radiances and ML radiances. In Figs. 11-13, each column shows GEMS, ML radiances and the

320 difference while the first and second rows show the radiances at representative wavelengths showing the smallest and the largest difference, respectively. Figure 11 shows the comparison results of the Defect 3 area, which presents the best performance compared to the Defect 1 and 2 areas. The difference in Fig. 11 is within $\pm$ 0.5% because the spectral gap of Defect 3 is narrower than the counterparts of Defects 1-2. For Defect 3, there is no scene dependence over the output wavelengths and the difference shows noise-like features and the spatial dependence originated from instrument artifacts.
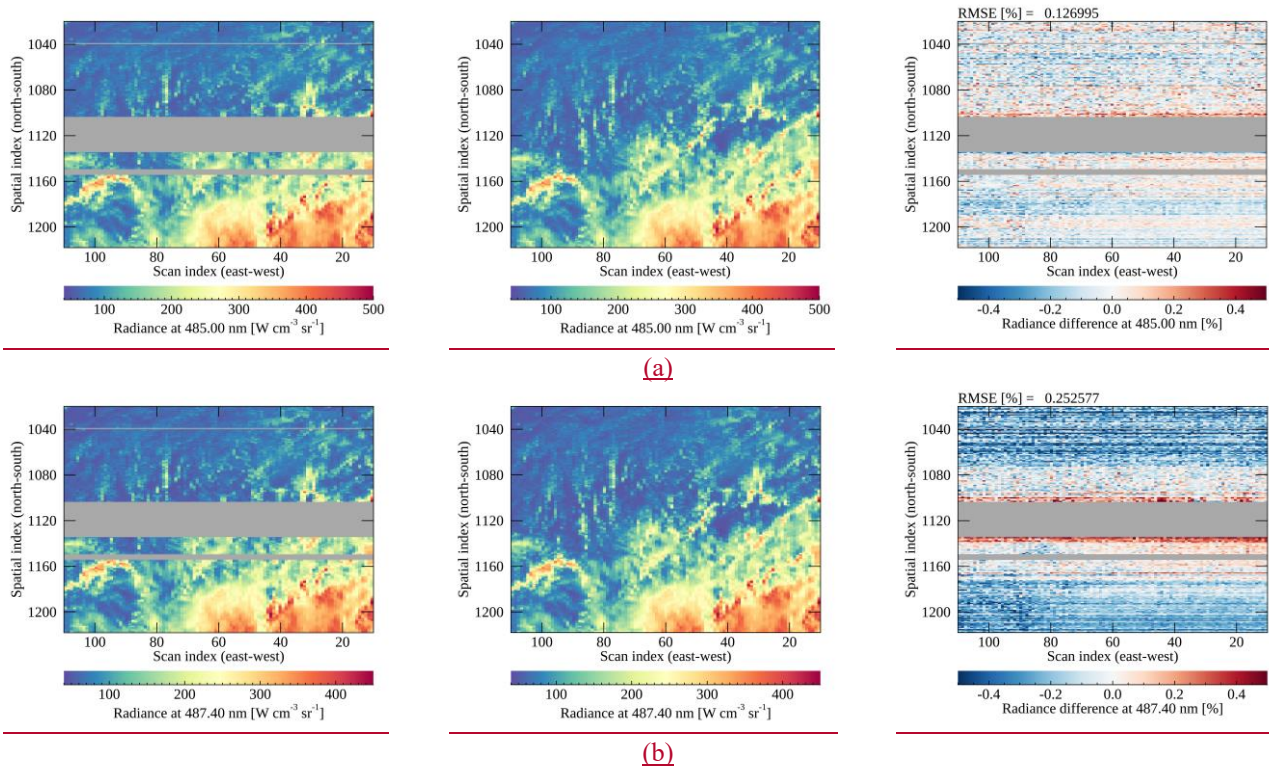
325 **Figure 11** The GEMS, ML radiances and the difference (from left to right) at the wavelengths presenting (a) the smallest and (b) the largest difference for the Defect 3 area. The difference is calculated between the ML and GEMS radiances divided by the latter in percent. Bad pixels are marked in dark gray and the color bar range is $\pm$ 0.5%. The unit of RMSE is in percent divided by the mean radiance.

Figure 12 shows the Defect 1 area where the ML radiances are within about 5% of the GEMS radiances. It also shows that dark targets (clear sky with small radiance) show a positive difference while bright targets (mostly cloudy sky with large radiances) show an opposite tendency. The tendencies are also found on the other dates for different angle conditions. It seems the applied machine learning model (PCA-Linear) might have its limitation in describing the non-linear relations of angle conditions, scene properties and radiances causing the difference of about 5%.
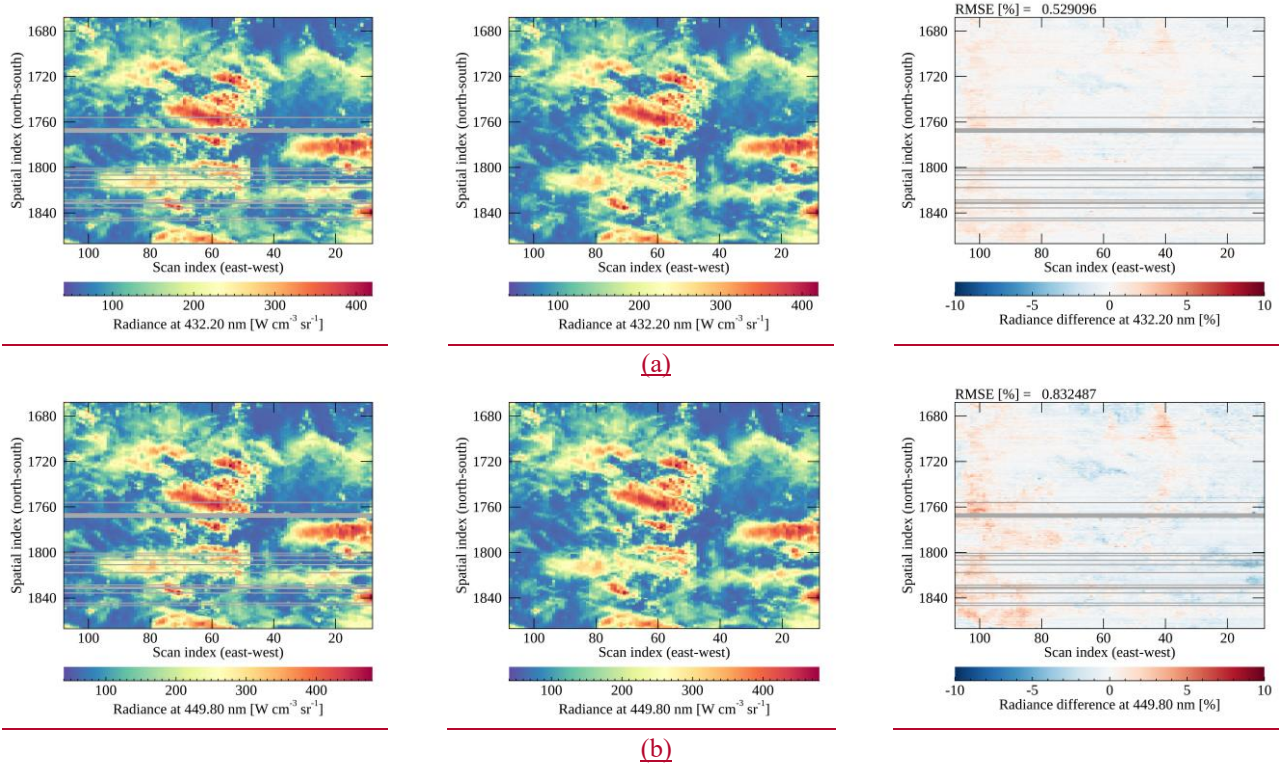
Figure 12 Same as Fig. 11 for the Defect 1 area with the color bar range of 10%.

For the Defect 2 area, it is clear that the information from radiances of wavelengths longer than 400 nm is insufficient to effectively reproduce the spectral features at shorter wavelengths (consistent results with Figs. 8-9). Both output spectral ranges of Defects 2-3 are around 100 nm but it seems the output radiances near 300 nm for Defect 2 need more information to be successfully reproduced. The stripping feature found in Fig. 13b becomes significant at 312 nm for the ML radiances on the contrary to the radiances at 357.2 nm in Fig.13a. The stripping feature seems to be added during the reproducing process especially for shorter wavelengths, and the reason is still unclear. Another distinct feature found in Fig. 13 is that the difference in northern parts is very large with the difference of 10%. We suspect that the reason might be the VZA effect considering that VZA increases at the northern parts in the area. Without angle conditions as the input parameters for the model, the difference becomes doubled at 312 nm presenting similar patterns with the difference in Fig. 13b. This indicates the angle effect can be emulated in the model by applying VZA and SZA as the input parameters, but it is not fully resolved especially for the radiances at shorter wavelengths.
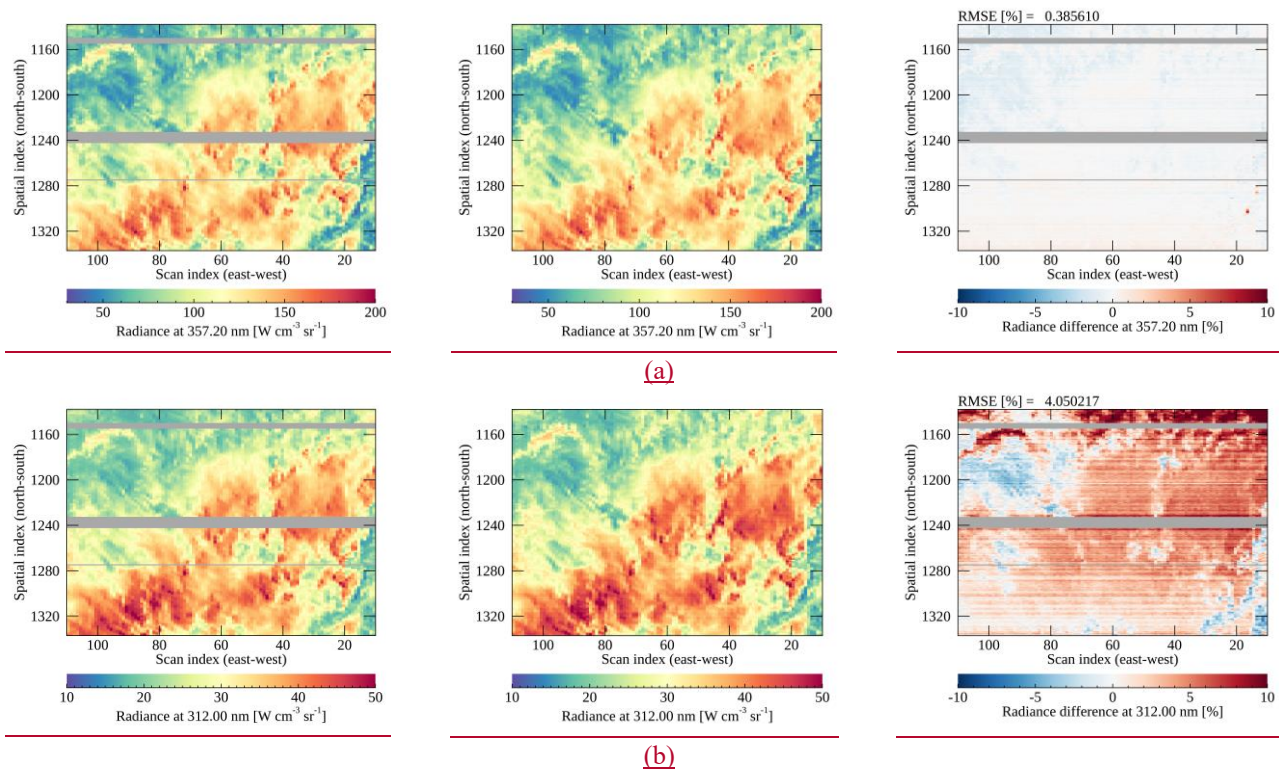
Figure 13 Same as Fig. 11 for the Defect 2 area with the color bar range of 10%.

A closer inspection is performed to analyze the general spectral features over target wavelengths. Within each defect area in Figs. 11-13, the collected spectra are divided into four groups considering that ML radiances could have different systematic biases depending on the scene brightness as shown in Fig. 11. Figure 14a shows that the ML radiances for the Defect 1 area over dark scenes have a positive bias while brighter scenes have a negative bias. It is interesting that the scene dependence is only significantly found for Defect 1. It should be noted that the y-axis range of Fig.14b is wider than the figures for Defects 1 and 3. Figure 14b indicates that the ML radiances are overestimated except for the very darker scenes especially at shorter wavelengths and it can be deduced that the complicated atmospheric effects involving clouds at the shorter wavelengths would affect the reproducing process. Figure 14c shows relatively large difference at the spectral peaks, but generally the difference is smaller than 0.2%

(a)	(b)	(c)
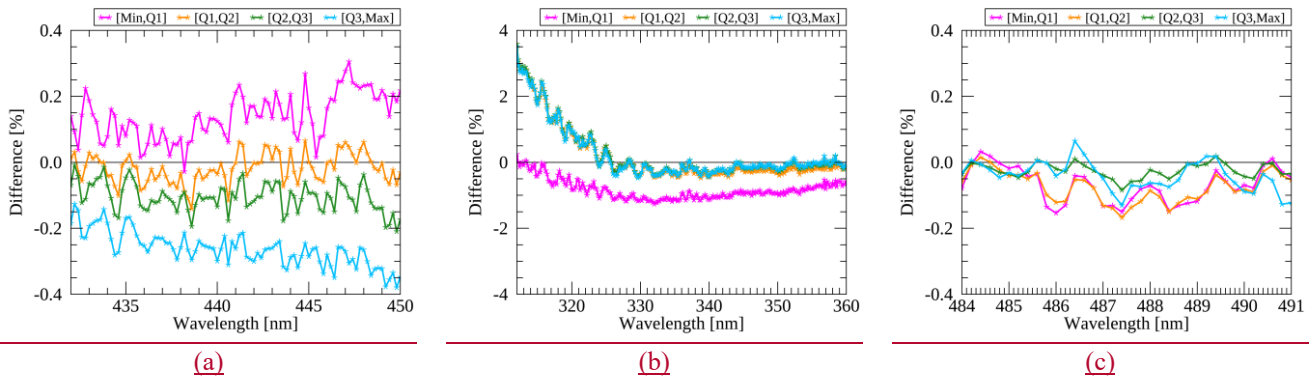
Figure 14 Mean difference between ML and GEMS radiances within the target area for (a) Defect 1, (b) Defect 2 and (c) Defect 3. Each color indicates the average for each quartile and Q1, Q2 and Q3 represent the first, second and third quartile, respectively. The difference is calculated between the ML and GEMS radiances divided by the latter in percent.

Besides the shorter wavelengths of Defect 2, the comparison between ML and GEMS radiances is presented by targeting Fraunhofer lines from 390 to 400 nm (see Fig. 14). The Ring effect caused by rotational Raman scattering can be found over the two peaks in Fig. 14a, which is generally known to be very small and largely affected by clouds (Joiner et al., 1995). Figure 14b shows that PCA-ANN reproduces the dominant features at the peaks very well on average within 0.6%, but it seems the difference increases with darker scenes where the Ring effect becomes stronger. This indicates that the ML radiances would need additional information to successfully reproduce the exact spectral features especially for the very small signals such as the Ring effect.

(a)	(b)
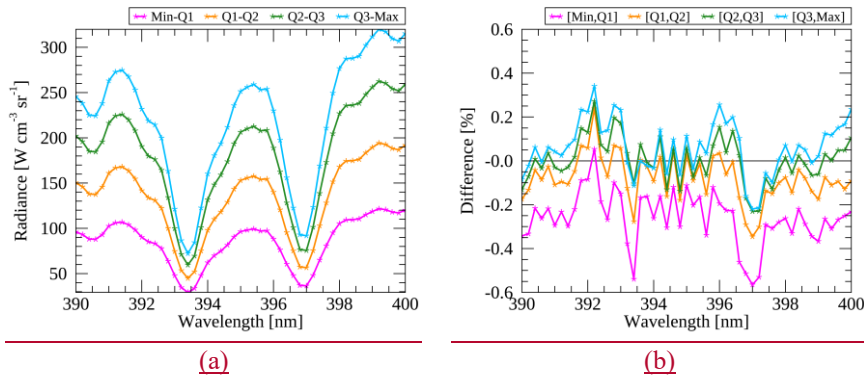
Figure 15 (a) Mean ML radiances (b) and the difference with GEMS radiances at Fraunhofer lines for the Defect 2 area. Each color indicates the average for each quartile and Q1, Q2 and Q3 represent the first, second and third quartile, respectively. The difference is calculated between the ML and GEMS radiances divided by the latter in percent.

3.2.2 PCA-based spectral analysis

As applied in the pre-processing step for the present research, PCA is a very useful tool to capture the meaningful variances and it has been widely used to retrieve environmental and surface properties (Horler and Ahern, 1986; Joiner et al., 2016; Li et al., 2013, 2015). To investigate further the spectral patterns, we apply PCA to GEMS radiances collected within each area in Fig. 11-13 at the target wavelengths (see Table 3). With PCA, various spectral patterns are compressed to PC scores and

this indicates that if a spectrum has disparate spectral patterns, the PC scores would also have distinct values when comparing with the PC scores of normal spectra. Figure 15 presents the PC scores of GEMS and ML radiances which are projected with

375 the identical eigenvector matrix (corresponding to **X** in Eq. 1) constructed from GEMS radiances. The Defect 3 area is targeted for the inspection which has the widest defective width along the north-south direction and the second PC scores are used for the analysis because the first PC scores represent mean radiances as discussed in Sect. 3.1.1. For the comparison, the radiances reproduced with spatial interpolation on the bad pixel area are projected together as shown in Fig.15a. As assumed, the PC scores from reproduced spectra with spatial interpolation show disparate values because the spectral patterns of the interpolated

380 spectra are inconsistent with the patterns of normal spectra. The ML radiances in Fig. 15b show spatially homogenous PC scores which indicates that the machine learning methods could properly reproduce the dominant spectral patterns, in the case of the second PC.

(a)   (b)
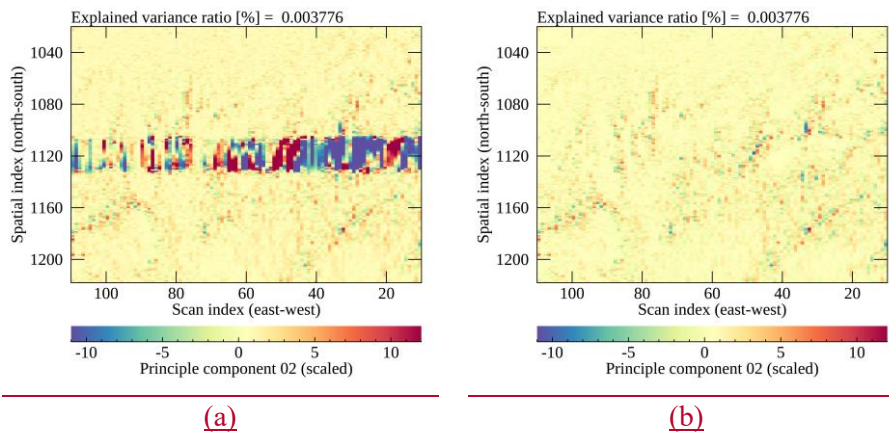
Figure 15. The second PC scores of (a) GEMS radiances and (b) ML radiances on the target area for Defect 3. The PC is scaled for clarity of presentation.

385   The dominant spectral patterns for each PC are presented in Fig. 16 with the eigenvector matrix constructed from GEMS radiances for the target wavelengths of Defects 1-3. Each color indicates the eigenvectors for the first-sixth PCs which determine the contribution of radiances at each wavelengths for each PC subspaces. Li et al. (2015) verifies that the leading PCs from the UV/VIS backscattered radiation (shorter than 360 nm) are highly correlated with dominant absorption features and surface properties and the trailing PCs might be associated with instrument artifacts and other unresolved spectral features

390 with PCA. Similarly, Fig. 16 shows that the eigenvector for the first PC corresponds to the mean spectrum and the eigenvector for the second-sixth PCs show dominant spectral patterns originated from absorption features of trace gases, surface properties and unresolved features. Considering that the dominant patterns could be identically found in the eigenvectors constructed from GEMS reflectance (not shown), it can be deduced that the patterns are extracted from the spectral features caused by atmospheric interactions rather than instrument artifacts.
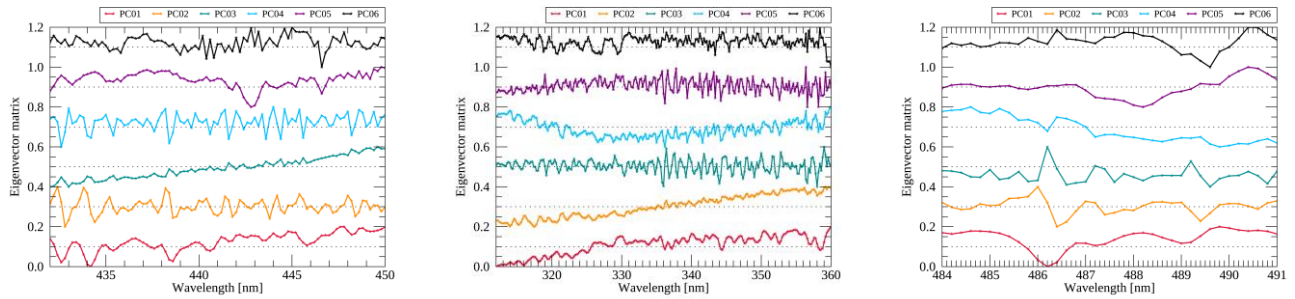
Figure 16 Eigenvector of the first-sixth PCs applied to GEMS radiances for the target wavelengths of (a) Defects 1, (b) Defect 2 and (c) Defect 3. All eigenvectors are scaled (min-max scaling) and shifted for clarity of presentation.

As presented in Table 4, the comparison of PC scores could indirectly provide the information on the similarity of the dominant patterns between ML and GEMS radiances with the correlation coefficient. The results show that the mean spectral pattern (the first PC) and some dominant patterns could be well reproduced with the suggested models, but other spectral features such as the second PC for Defect 2 have difficulty obtaining valid information from input radiances for accurate reproduction. The contribution to the original radiances from each PC might be very small except for the first PC because even the leading PCs have small explained variance ratio for hyperspectral data in UV/VIS spectrum. However, considering the results in Figs. 14-15, it would be enough to determine the exact spectral patterns significantly related to the important information for the retrieval process, which needs to be investigated further.

Table 4. Correlation coefficient between PC scores of GEMS and ML radiances for the target areas of Defects 1-3 with the exception of bad pixels.

Defects	PC 01	PC 02	PC 03	PC 04	PC 05	PC 06
Defect 1	0.9999	0.9976	0.8172	0.9779	0.6846	0.6609
Defect 2	0.9999	0.8129	0.9876	0.4294	0.7035	0.5046
Defect 3	0.9999	0.9962	0.9787	0.6644	0.5399	0.2649

4 Conclusions

GEMS is an environmental sensor measuring hyperspectral radiances from 300 to 500 nm in the Asia-Pacific region for timely atmospheric monitoring. During the IOT of GEMS, one of calibration issues was found that erroneous values of bad pixels on the detector array are not properly replaced with spatial interpolation, the current operational method of GEMS. It is clear that when the bad pixel area is too large, the spatial interpolation tends to cause high interpolation error especially for a scene having large spatial inhomogeneity (i.e. cloud edges). The high interpolation error of bad pixels could affect to the retrieval process, which causes horizontal discontinuity at a certain latitude for the retrieval of Level 2 products.

To resolve the issue, this study suggests machine learning methods using PCA-ANN and PCA-Linear to fill in the the spectral gaps caused by bad pixels, denoted as Defects 1-3 in this study. The basic assumption of this approach is that radiances of a spectrum have strong linear and non-linear relations, which could be emulated with the ANN and multivariate linear regression. The spectral range of output radiances corresponds to the wavelengths of bad pixels, while the input radiances

correspond to the rest part of a spectrum for Defects 1-3, respectively. Considering that input radiances have strong linear relations, dimensionality reduction with PCA is applied in the pre-processing step to reduce linear relations of input radiances
420 and to increase computational efficiency of training process.

In the results, PCA-Linear model presents smaller prediction errors for the defective region having strong linear relations between input and output radiances (Defect 1) or having a narrower spectral gap (Defect 3). The PCA-ANN model is better for the output radiances having strong non-linear relations with input radiances (Defect 2). The narrower the spectral range of output radiances is, the smaller the prediction error is because the prediction error of Defect 3 is around 0.5%, while
425 it is around 5% for Defects 1 and 2 except for the shorter wavelengths around 300 nm. The comparison results between measured and reproduced radiances show that the dominant spectral patterns could be successfully reproduced for the spectral gap-filling mostly within 5%, while the spectral patterns determined by very small signals such as the Ring effect would be insufficiently reproduced with the suggested methods. The extracted spectral patterns using PCA also present the similar results showing highly correlated PC scores for the first PC for Defect 1-3 regardless of the models, while the PCs determining subtle
430 spectral features are relatively less correlated especially for Defect 1-2.

~~When the trained model is applied to the actual bad pixels, the spectral gap of bad pixels is properly replaced presenting continuous spectral features especially for Defect 2 and 3. The bad pixel replacement with PCA-Linear and spatial interpolation for Defect 1 is almost same considering the narrower spatial gap of Defect 1.~~

To apply the methods in operation, however, it needs to be updated further to solve the following issues. The machine
435 learning model, especially the PCA-ANN model, becomes highly unstable when measurement characteristics of training and test data significantly change. If measurements have high seasonal dependence, then the time lag between training and test data should be as shorter as possible to guarantee that both data are sampled from an identical population considering the basic premise of ANN. It is empirically found that the time lag between training and test data should not be over two weeks for GEMS which could be technically demanding in operation. Secondly, the radiance at shorter wavelengths (around 325 nm) of
440 Defect 2 has high prediction error of over 5%, which is higher than the level of radiometric calibration accuracy of GEMS (4%). To increase prediction accuracy at strong absorption lines and describe precise spectral features, additional information would be needed besides the spectral relations of radiances in a spectrum.~~it needs to be updated further.~~

Considering that the number of bad pixels would increase in operation as did in Ozone Mapping and Profiler Suite (OMPS) (Seftor et al., 2014), an efficient way of replacing bad pixels would be necessary for the long-term operation of GEMS.
445 It is also highly possible that an unexpected issue could occur such as the row-anomaly of Ozone Monitoring Instrument (OMI) (Schenkeveld et al., 2017), machine learning methods suggested in this study can be a useful tool for filling in ~~the~~ a spectral gap and increasing the number of data reserving measurement characteristics of the sensor.

Author contribution

M.-H.A. conceptualized and supervised the study; Y.L. conducted the research, performed the experiments and prepared the manuscript; M.K. contributed to the editing of the manuscript and developing methodology. M.E. contributed to the pre-processing of raw data.

Competing interests

The authors declare that they have no conflict of interest.

Acknowledgements

We would like to thank the Environment Satellite Center (ESC) of National Institute of Environmental Research (NIER) for providing GEMS Level 0-2 data.

Financial support

This research was supported by Basic Science Research Program through the National Research Foundation of Korea(NRF) funded by the Ministry of Education(2018R1A6A1A08025520).

References

Bajorski, P.: Statistical inference in PCA for hyperspectral images, IEEE J. Sel. Top. Signal Process., 5(3), 438–445, doi:10.1109/JSTSP.2011.2105244, 2011.

Bak, J., Baek, K. H., Kim, J. H., Liu, X., Kim, J. and Chance, K.: Cross-evaluation of GEMS tropospheric ozone retrieval performance using OMI data and the use of an ozonesonde dataset over East Asia for validation, Atmos. Meas. Tech., 12(9), 5201–5215, doi:10.5194/amt-12-5201-2019, 2019.

Boersma, K. F., Eskes, H. J. and Brinksma, E. J.: Error analysis for tropospheric NO2 retrieval from space, J. Geophys. Res. D Atmos., 109(4) [online] Available from: https://agupubs.onlinelibrary.wiley.com/doi/abs/10.1029/2003jd003962 (Accessed 20 September 2019), 2004.

Boldrini, B., Kessler, W., Rebner, K. and Kessler, R.: Hyperspectral imaging: a review of best practice, performance and pitfalls for inline and online applications, J. Near Infrared Spectrosc., 20(5), 438, doi:10.1255/jnirs.1003, 2012.

Bovensmann, H., Burrows, J. P., Buchwitz, M., Frerick, J., Noël, S., Rozanov, V. V., Chance, K. V. and Goede, A. P. H.: SCIAMACHY: Mission objectives and measurement modes, J. Atmos. Sci., 56(2), 127–150, doi:10.1175/1520-0469(1999)056<0127:SMOAMM>2.0.CO;2, 1999.

Burger, J.: Replacement of Hyperspectral Image Bad Pixels, NIR news, 20(7), 19–21, doi:10.1255/nirn.1151, 2009.

475 Choi, H., Liu, X., Gonzalez Abad, G., Seo, J., Lee, K.-M. and Kim, J.: A Fast Retrieval of Cloud Parameters Using a Triplet of Wavelengths of Oxygen Dimer Band around 477 nm, Remote Sens., 13(1), 152, doi:10.3390/rs13010152, 2021.

Cybenko, G.: Approximation by superpositions of a sigmoidal function, Math. Control. Signals, Syst., 2(4), 303–314, doi:10.1007/BF02551274, 1989.

Dorvlo, A. S. S., Jervase, J. A. and Al-Lawati, A.: Solar radiation estimation using aritificial neural networks, Appl. Energy,

480 71(4), 307–319, doi:10.1016/S0306-2619(02)00016-8, 2002.

Fischer, A. D., Downes, T. V. and Leathers, R.: Median spectral-spatial bad pixel identification and replacement for hyperspectral SWIR sensors, in Algorithms and Technologies for Multispectral, Hyperspectral, and Ultraspectral Imagery XIII, vol. 6565, edited by S. S. Shen and P. E. Lewis, p. 65651E, SPIE., 2007.

Gewali, U. B., Monteiro, S. T. and Saber, E.: Machine learning based hyperspectral image analysis: A survey, arXiv, 2018.

485 Goetz, A. F. H., Vane, G., Solomon, J. E. and Rock, B. N.: Imaging spectrometry for earth remote sensing, Science (80-.)., 228(4704), 1147–1153, doi:10.1126/science.228.4704.1147, 1985.

Hedelt, P., Efremenko, D. S., Loyola, D. G., Spurr, R. and Clarisse, L.: Sulfur dioxide layer height retrieval from Sentinel-5 Precursor/ TROPOMI using FP_ILM, Atmos. Meas. Tech, 12, 5503–5517, doi:10.5194/amt-12-5503-2019, 2019.

Horler, D. N. and Ahern, F. J.: Forestry information content of thematic mapper data, Int. J. Remote Sens., 7(3), 405–428,

490 doi:10.1080/01431168608954695, 1986.

Hornik, K., Stinchcombe, M. and White, H.: Multilayer feedforward networks are universal approximators, Neural Networks, 2(5), 359–366, doi:10.1016/0893-6080(89)90020-8, 1989.

Howell, S. B.: CCD imaging, in Handbook of CCD Astronomy, pp. 66–101, Cambridge University Press, Cambridge., 2006.

Joiner, J., Bhartia, P. K., Cebula, R. P., Hilsenrath, E., McPeters, R. D. and Park, H.: Rotational Raman scattering (Ring

495 effect) in satellite backscatter ultraviolet measurements, Appl. Opt., 34(21), 4513, doi:10.1364/AO.34.004513, 1995.

Joiner, J., Yoshida, Y., Guanter, L. and Middleton, E. M.: New methods for the retrieval of chlorophyll red fluorescence from hyperspectral satellite instruments: Simulations and application to GOME-2 and SCIAMACHY, Atmos. Meas. Tech., 9(8), 3939–3967, doi:10.5194/amt-9-3939-2016, 2016.

Kang, M., Ahn, M. H., Liu, X., Jeong, U. and Kim, J.: Spectral calibration algorithm for the geostationary environment

500 monitoring spectrometer (Gems), Remote Sens., 12(17), 1–17, doi:10.3390/rs12172846, 2020.

Kieffer, H. H.: Detection and correction of bad pixels in hyperspectral sensors, in Hyperspectral Remote Sensing and Applications, vol. 2821, edited by S. S. Shen, pp. 93–108, SPIE., 1996.

Kim, G., Choi, Y. S., Park, S. S. and Kim, J.: Effect of solar zenith angle on satellite cloud retrievals based on O2–O2 absorption band, Int. J. Remote Sens., 42(11), 4224–4240, doi:10.1080/01431161.2021.1890267, 2021.

505 Kim, J., Jeong, U., Ahn, M. H., Kim, J. H., Park, R. J., Lee, H., Song, C. H., Choi, Y. S., Lee, K. H., Yoo, J. M., Jeong, M. J., Park, S. K., Lee, K. M., Song, C. K., Kim, S. W., Kim, Y. J., Kim, S. W., Kim, M., Go, S., Liu, X., Chance, K., Miller, C. C., Al-Saadi, J., Veihelmann, B., Bhartia, P. K., Torres, O., Abad, G. G., Haffner, D. P., Ko, D. H., Lee, S. H., Woo, J. H.,

Chong, H., Park, S. S., Nicks, D., Choi, W. J., Moon, K. J., Cho, A., Yoon, J., Kim, S. kyun, Hong, H., Lee, K., Lee, H., Lee, S., Choi, M., Veefkind, P., Levelt, P. F., Edwards, D. P., Kang, M., Eo, M., Bak, J., Baek, K., Kwon, H. A., Yang, J., Park,

510 J., Han, K. M., Kim, B. R., Shin, H. W., Choi, H., Lee, E., Chong, J., Cha, Y., Koo, J. H., Irie, H., Hayashida, S., Kasai, Y., Kanaya, Y., Liu, C., Lin, J., Crawford, J. H., Carmichael, G. R., Newchurch, M. J., Lefer, B. L., Herman, J. R., Swap, R. J., Lau, A. K. H., Kurosu, T. P., Jaross, G., Ahlers, B., Dobber, M., McElroy, C. T. and Choi, Y.: New era of air quality monitoring from space: Geostationary environment monitoring spectrometer (GEMS), Bull. Am. Meteorol. Soc., 101(1), E1–E22, doi:10.1175/BAMS-D-18-0013.1, 2020.

515 Kingma, D. P. and Ba, J. L.: Adam: A method for stochastic optimization, in 3rd International Conference on Learning Representations, ICLR 2015 - Conference Track Proceedings, International Conference on Learning Representations, ICLR. [online] Available from: https://arxiv.org/abs/1412.6980v9 (Accessed 7 May 2021), 2015.

Le, T., Liu, C., Yao, B., Natraj, V. and Yung, Y. L.: Application of machine learning to hyperspectral radiative transfer simulations, J. Quant. Spectrosc. Radiat. Transf., 246, 106928, doi:10.1016/j.jqsrt.2020.106928, 2020.

520 Li, C., Joiner, J., Krotkov, N. A. and Bhartia, P. K.: A fast and sensitive new satellite SO2 retrieval algorithm based on principal component analysis: Application to the ozone monitoring instrument, Geophys. Res. Lett., 40(23), 6314–6318, doi:10.1002/2013GL058134, 2013.

Li, C., Joiner, J., Krotkov, N. A. and Dunlap, L.: A new method for global retrievals of HCHO total columns from the Suomi National Polar-orbiting Partnership Ozone Mapping and Profiler Suite, Geophys. Res. Lett., 42(7), 2515–2522,

525 doi:10.1002/2015GL063204, 2015.

Liu, X., Smith, W. L., Zhou, D. K. and Larar, A.: Principal component-based radiative transfer model for hyperspectral sensors: Theoretical concept, Appl. Opt., 45(1), 201–209, doi:10.1364/AO.45.000201, 2006.

Lo´pez-Alonso, J. M. and Alda, J.: Bad pixel identification by means of principal components analysis, Opt. Eng., 41(9), 2152, doi:10.1117/1.1497397, 2002.

530 Loyola, D. G., Gimeno García, S., Lutz, R., Argyrouli, A., Romahn, F., Spurr, R. J. D., Pedergnana, M., Doicu, A., Molina García, V. and Schüssler, O.: The operational cloud retrieval algorithms from TROPOMI on board Sentinel-5 Precursor, Atmos. Meas. Tech, 11, 409–427, doi:10.5194/amt-11-409-2018, 2018.

Ludewig, A., Kleipool, Q., Bartstra, R., Landzaat, R., Leloux, J., Loots, E., Meijering, P., Van Der Plas, E., Rozemeijer, N., Vonk, F. and Veefkind, P.: In-flight calibration results of the TROPOMI payload on board the Sentinel-5 Precursor satellite,

535 Atmos. Meas. Tech., 13(7), 3561–3580, doi:10.5194/amt-13-3561-2020, 2020.

Manolakis, D., Pieper, M., Truslow, E., Lockwood, R., Weisner, A., Jacobson, J. and Cooley, T.: Longwave infrared hyperspectral imaging: Principles, progress, and challenges, IEEE Geosci. Remote Sens. Mag., 7(2), 72–100, doi:10.1109/MGRS.2018.2889610, 2019.

Marchetti, Y., Rosenberg, R. and Crisp, D.: Classification of Anomalous Pixels in the Focal Plane Arrays of Orbiting Carbon

540 Observatory-2 and -3 via Machine Learning, Remote Sens., 11(24), 2901, doi:10.3390/rs11242901, 2019.

Nwankpa, C., Ijomah, W., Gachagan, A. and Marshall, S.: Activation Functions: Comparison of trends in Practice and Research for Deep Learning, arXiv [online] Available from: http://arxiv.org/abs/1811.03378 (Accessed 8 May 2021), 2018.

Pan, C., Weng, F. and Flynn, L.: Spectral Performance and Calibration of the Suomi NPP OMPS Nadir Profiler Sensor, Earth Sp. Sci., 4(12), 737–745, doi:10.1002/2017EA000336, 2017.

545   Pan, C., Zhou, L., Cao, C., Flynn, L. and Beach, E.: Suomi-NPP OMPS Nadir mapper's operational SDR performance, IEEE Trans. Geosci. Remote Sens., 57(2), 1015–1024, doi:10.1109/TGRS.2018.2864125, 2019.

Pan, C., Yan, B., Cao, C., Flynn, L., Xiong, X., Beach, E. and Zhou, L.: Performance of OMPS Nadir Profilers' Sensor Data Records, IEEE Trans. Geosci. Remote Sens., 1–9, doi:10.1109/tgrs.2020.3026586, 2020.

Rankin, B. M., Broadwater, J. B. and Smith, M.: Anomalous pixel replacement and spectral quality algorithm for longwave

550   infrared hyperspectral imagery, Int. Geosci. Remote Sens. Symp., 2018-July, 4316–4319, doi:10.1109/IGARSS.2018.8517461, 2018.

Schenkeveld, V. M. E., Jaross, G., Marchenko, S., Haffner, D., Kleipool, Q. L., Rozemeijer, N. C., Veefkind, J. P. and Levelt, P. F.: In-flight performance of the Ozone Monitoring Instrument, Atmos. Meas. Tech., 10(5), 1957–1986, doi:10.5194/amt-10-1957-2017, 2017.

555   Schläpfer, D., Nieke, J. and Itten, K. I.: Spatial PSF nonuniformity effects in airborne pushbroom imaging spectrometry data, IEEE Trans. Geosci. Remote Sens., 45(2), 458–468, doi:10.1109/TGRS.2006.886182, 2007.

Seftor, C. J., Jaross, G., Kowitt, M., Haken, M., Li, J. and Flynn, L. E.: Postlaunch performance of the Suomi National Polar-orbiting Partnership Ozone Mapping and Profiler Suite (OMPS) nadir sensors, J. Geophys. Res. Atmos., 119(7), 4413–4428, doi:10.1002/2013JD020472, 2014.

560   Taylor, M., Kosmopoulos, P. G., Kazadzis, S., Keramitsoglou, I. and Kiranoudis, C. T.: Neural network radiative transfer solvers for the generation of high resolution solar irradiance spectra parameterized by cloud and aerosol parameters, J. Quant. Spectrosc. Radiat. Transf., 168, 176–192, doi:10.1016/j.jqsrt.2015.08.018, 2016.

Wu, W., Liu, X., Xiong, X., Li, Y., Yang, Q., Wu, A., Kizer, S. and Cao, C.: An Accurate Method for Correcting Spectral Convolution Errors in Intercalibration of Broadband and Hyperspectral Sensors, J. Geophys. Res. Atmos., 123(17), 9238–

565   9255, doi:10.1029/2018JD028585, 2018.

Zarzalejo, L. F., Ramirez, L. and Polo, J.: Artificial intelligence techniques applied to hourly global irradiance estimation from satellite-derived cloud index, in Energy, vol. 30, pp. 1685–1697, Elsevier Ltd., 2005.

Zhen, Y. and Li, C.: Cross-Domain Knowledge Transfer Using Semi-supervised Classification, Lect. Notes Comput. Sci. (including Subser. Lect. Notes Artif. Intell. Lect. Notes Bioinformatics), 5360 LNAI, 362–371, doi:10.1007/978-3-540-

570   89378-3_36, 2008.

Zhu, S., Lei, B. and Wu, Y.: Retrieval of hyperspectral surface reflectance based on machine learning, Remote Sens., 10(2), 1–15, doi:10.3390/rs10020323, 2018.